Reevaluation of the Bulk Exchange Coefficient for Humidity at Sea during Unstable and Neutral Conditions

ERIK SAHLÉE, ANN-SOFI SMEDMAN, ULF HÖGSTRÖM, AND ANNA RUTGERSSON

Department of Earth Sciences, Uppsala University, Uppsala, Sweden

(Manuscript received 28 January 2007, in final form 4 April 2007)

ABSTRACT

Processes influencing the air–sea exchange of humidity during unstable and neutral stratification were studied using tower measurements from the island of Östergarnsholm in the Baltic Sea. For small air–sea temperature differences, the neutral exchange coefficient for humidity C_{EN} was found to increase with increasing wind speed, attaining a value of approximately 1.8×10^{-3} at 13 m s^{-1}. The high C_{EN} values were observed during situations when the characteristics of the turbulence structure differed from what would be expected from traditional theory. Results from spectral analysis point to a situation in which the vertical transport of humidity is dominated by smaller-scale eddies. Quadrant analysis showed that these eddies enhance the humidity flux by bringing down drier air from layers aloft. These findings are consistent with recent analyses of the neutral boundary layer in which a change of turbulence regime has been observed. The conclusion is made that this dynamic effect accounts for the observed increase in C_{EN}. Here, C_{EN} was calculated using a wave-dependent normalized wind gradient, which had the effect of reducing the value by about 10% during swell relative to calculations using a non-wave-dependent normalized wind gradient.

1. Introduction

In recent decades there have been significant efforts to increase our understanding of the turbulent exchange of momentum, heat, and moisture between the ocean and the atmosphere. Research concerning this exchange is important, not only from a basic research point of view, but also since boundary conditions in models are dependent on a correct description of the turbulent exchange at the surface. If correctly applied, improved knowledge of the turbulent exchange will make model descriptions of processes at the air–sea interface more accurate, resulting in better model predictions.

Meteorological models commonly use a bulk approach when calculating turbulent fluxes at the sea surface. This is a convenient method that relates fluxes to mean gradients and wind speed through an exchange coefficient. The success of the bulk approach lies in the ability to correctly describe the exchange coefficients, which has been the main objective of numerous field experiments (see section 5). The results from the field experiments have improved our knowledge about the exchange coefficients; however, there is more to learn. For instance, recently Zhang et al. (2006) showed improved model predictions of storm intensity by including sea spray effects in the calculations.

In addition, field experiments (e.g., Smedman et al. 1999, 2003; Rutgersson et al. 2001a) as well as model studies (Sullivan et al. 2004) have shown that the marine boundary layer is strongly influenced by the wave field. In the presence of long waves an upward directed component of the momentum flux is induced, which alters the wind and turbulence profiles. Guo Larsén et al. (2004) studied the wind profile during different wave conditions and presented new expressions of the nondimensional wind gradient. A changed nondimensional wind gradient also influences the exchange coefficients. In Smedman et al. (2007b) the exchange coefficient for sensible heat was shown to decrease in the presence of swell-dominated wave fields. A similar effect is expected for the exchange coefficient for latent heat, which is investigated in the present paper.

Yet another process influencing the air–sea exchange was presented in Smedman et al. (2007a,b). It was shown that the exchange coefficient for sensible heat

Corresponding author address: Erik Sahlée, Department of Earth Sciences, Uppsala University, Uppsala, Sweden.
E-mail: erik.sahlee@met.uu.se

DOI: 10.1175/2007JPO3754.1

was greatly enhanced during near-neutral conditions (slightly unstable). This was found to be an effect of the development of a special turbulence regime termed the unstable very close to neutral (UVCN) regime. The UVCN regime is characterized by surface-layer-scale eddies originating as detached eddies in layers above the surface layer. When these eddies are formed they move downward, transporting colder air to the surface, which enhances the sensible heat flux. In this study the effect of the UVCN regime on the exchange coefficient for the latent heat flux is investigated.

Present state-of-the-art knowledge of surface fluxes during different stratifications is implemented in the Coupled Ocean–Atmosphere Response Experiment (COARE) 3.0 algorithm (Fairall et al. 2003). The COARE algorithm is developed from surface renewal theory and is used to calculate the surface fluxes. Here it is used as a reference calculation. Surface renewal theory, as well as the COARE algorithm, is described in more detail in sections 2b and 2c.

The measurement site and instrumentation are presented in section 3. Section 4 presents the results, which are discussed and compared with previous findings in section 5. Conclusions are presented in section 6.

2. Theory

a. Neutral exchange coefficients

The transfer coefficients for latent and sensible heat, C_E and C_H, are defined through the bulk formulas

$$C_E = \frac{\overline{w'q'}}{(U_{10} - U_0)(q_w - q_{10})} \quad \text{and} \tag{1a}$$

$$C_H = \frac{\overline{w'\theta'}}{(U_{10} - U_0)(\theta_w - \theta_{10})}, \tag{1b}$$

where $\overline{w'q'}$ is the turbulent flux of specific humidity (m s^{-1} kg kg^{-1}), $\overline{w'\theta'}$ is the turbulent flux of potential temperature (m s^{-1} K), U_{10} is the mean wind speed at 10 m and U_0 is the mean wind speed at the sea surface (m s^{-1}), q_w is the specific humidity at the water surface (kg kg^{-1}; i.e., the saturation humidity at the sea surface temperature), q_{10} is the specific humidity at 10 m, θ_w is the potential temperature at the sea surface (K), and θ_{10} is the potential temperature at 10 m.

During conditions for which the Monin–Obukhov similarity theory (MOST) applies, the exchange coefficients can be reduced to their neutral counterparts, C_{EN} and C_{HN}. This is done to remove the effects of stability and make it easier to compare measurements.

MOST states that in a constant flux layer and over a horizontally homogeneous surface, nondimensional profile functions can be formed as unique functions of the stability parameter, z/L. The normalized profile functions for humidity, temperature, and wind speed are as follows:

$$\phi_q(z/L) = \frac{\partial q}{\partial z}\frac{kz}{q_*}, \tag{2a}$$

$$\phi_h(z/L) = \frac{\partial \theta}{\partial z}\frac{kz}{\theta_*}, \quad \text{and} \tag{2b}$$

$$\phi_m(z/L) = \frac{\partial u}{\partial z}\frac{kz}{u_*}, \tag{2c}$$

where $q_* = -\overline{w'q'}/u_*$ is the scaling variable for humidity, $\theta_* = -\overline{w'\theta'}/u_*$ is the scaling variable for temperature, z is the height above the surface (m), $L = -(u_*^3 T_0)/(gk\overline{w'\theta_v'})$ is the Obukhov length (m), k is the von Kármán constant ($\approx$0.4), u_* is the friction velocity (m s^{-1}), and $\overline{w'\theta_v'}$ (m s^{-1} K) is the turbulent flux of virtual potential temperature.

The surface-layer profiles of humidity, temperature, and wind speed are obtained by vertical integration of Eqs. (2a)–(2c):

$$q - q_0 = \frac{q_*}{k}[\ln(z/z_{0q}) - \psi_q], \tag{3}$$

$$\theta - \theta_0 = \frac{\theta_*}{k}[\ln(z/z_{0t}) - \psi_h], \quad \text{and} \tag{4}$$

$$U - U_0 = \frac{u_*}{k}[\ln(z/z_0) - \psi_m], \tag{5}$$

where z_0, z_{0q}, and z_{0t} are the roughness lengths for wind speed, humidity, and temperature, respectively, in other words the lower limit of the logarithmic profiles. Here ψ_x represents the integrated nondimensional profile functions,

$$\psi_x(\zeta) = \int_0^{z/L} (1 - \phi_x\zeta)/\zeta \, d\zeta, \tag{6}$$

where $\zeta = z/L$ and $x = q$, h, or m.

The absence of a strong surface current leaves U_0 to be equal to the surface drift velocity, which is 1%–2% of the wind speed, so assuming $U_0 = 0$ is reasonable. Substitution of Eqs. (3)–(5) into Eqs. (1a) and (1b) yields

$$C_E = \left[\frac{k}{\ln(z/z_0) - \psi_m}\right]\left[\frac{k}{\ln(z/z_{0q}) - \psi_q}\right] \quad \text{and} \tag{7a}$$

$$C_H = \left[\frac{k}{\ln(z/z_0) - \psi_m}\right]\left[\frac{k}{\ln(z/z_{0t}) - \psi_h}\right]. \tag{7b}$$

It is traditionally assumed that $\phi_m = \phi_h = \phi_q \approx 1$ for $z/L = 0$ (cf. below), which makes $\psi_m = \psi_q = \psi_h \approx 0$ during neutral conditions. We then obtain the neutral exchange coefficient for latent and sensible heat:

$$C_{\mathrm{EN}} = \frac{k^2}{[\ln(z/z_0)][\ln(z/z_{0q})]} \quad \text{and} \tag{8a}$$

$$C_{\mathrm{HN}} = \frac{k^2}{[\ln(z/z_0)][\ln(z/z_{0t})]}. \tag{8b}$$

By knowing ψ_m, ψ_h, and ψ_q, the roughness lengths z_0, z_{0q}, and z_{0t} can be calculated from Eqs. (3)–(5) if the turbulent fluxes, U_{10}, and the bulk differences, $q - q_0$ and $\theta - \theta_0$, are measured.

This method is applicable only during conditions for which MOST is valid. However, as shown in Smedman et al. [2007b; cf. section 2d(2)] MOST is not valid during unstable conditions very close to neutral. An apparent z_{0q} value is used for this stability range, identified using $L < -150$ m, by setting $\psi_q = 0$ in Eq. (3). As an effect, C_{EN} is enhanced by approximately 2.5% relative to calculations using the traditional ψ_q value.

Edson et al. (2004) showed that $\phi_h = \phi_q$. The following expression from Högström (1988) is used:

$$\phi_h = 0.95(1 - 11.6z/L)^{-1/2}. \tag{9}$$

b. The influence of the sea state

According to the findings of Guo Larsén et al. (2004), the status of the wave field should be considered when calculating the ϕ_m functions. Thus, the sea state will have an indirect influence on the exchange coefficients. The sea state is categorized using the wave age parameter, here defined as c_p/U_{10}, where c_p is the phase speed of the waves at the peak frequency in the wave spectra.

When the wave age is larger than 1.2, long waves or swell dominate the sea surface. A wave age between 0.8 and 1.2 represents a mature sea, a mix of swell and shorter waves. Conditions with a wave age less than 0.8 are called growing sea; that is, the sea surface is dominated by waves generated by the local wind.

In the presence of long waves, the wind gradient is modified as a result of wave-induced, upward-directed momentum flux (Sullivan et al 2004; Smedman et al. 2003). Guo Larsén et al. (2004) show that during unstable atmospheric conditions, the ϕ_m function decreases when the proportion of long waves increases. By fitting a curve to measured ϕ_m values as a function of z/L, they obtain the following expressions: For a mature sea when $-0.5 < z/L < 0$,

$$\phi_m = 1 - (-2z/L)^{1/2}; \tag{10a}$$

For a mature sea with $z/L < -0.5$,

$$\phi_m = 0. \tag{10b}$$

For swell when $-1 < z/L < 0$,

$$\phi_m = 1 - (-3z/L)^{1/2}; \tag{10c}$$

For swell with $z/L < -1$,

$$\phi_m = -0.73. \tag{10d}$$

Note that these modifications are derived for wind following unidirectional swell, a situation commonly encountered in limited-sized basins like the Baltic Sea, but presumably much less common in the open oceans. This is due to the fact that only one source region to swell, that is, low pressure system, fits within the Baltic Sea area at a time. The geometry then limits the swell direction to mainly south–north, which also is the wind direction sector used for over water fetch measurements at the Östergarnsholm site.

For growing sea during unstable conditions, there is little difference between the ϕ_m function obtained over sea and that obtained over land. For such conditions, the ϕ_m function from Högström (1996) is used:

$$\phi_m = (1 - 19z/L)^{-1/4}. \tag{11}$$

During swell and mature sea, C_{EN} is calculated using the wave-dependent ϕ_m function. A comparison to calculations with C_{EN} using a traditional ϕ_m function is presented in section 4.

c. Surface renewal theory

Surface renewal theory describes the physical processes governing the exchange at the air–sea interface. In this framework, the exchange at the air–sea interface is largely controlled by the diffusive transport in the thin interfacial sublayer, which forms a bottleneck for the air–sea exchange (for a thorough description see, e.g., Brutsaert 1975). Several surface flux algorithms are more or less based on surface renewal theory, for example, the Liu–Katsaros–Businger model (Liu et al. 1979), the COARE algorithm [see Fairall et al. (1996) for a description of version 2.5], and the model of Clayson et al. (1996). A common finding of these studies is that the exchange coefficients generally decrease slightly with increasing wind speed.

The latest version (3.0) of the COARE algorithm, presented in Fairall et al. (2003), is modified relative to previous versions, though it can still be considered a surface renewal model. By tuning the parameterizations of z_0 and z_{0q} to experimental data, C_{EN} calculated with COARE 3.0 is shown to increase slightly with increasing wind speed.

d. Limitations of surface renewal theory

As long ago as 1979, Liu et al. (1979) stated that the application of surface renewal theory is limited to low and moderate wind speeds. At higher wind speeds, the thin interfacial sublayer is disturbed by wave breaking, which questions the applicability of classical surface renewal theory, and thus additional physical processes have to be considered. Two possible factors that could affect the exchange coefficient are studied in detail in this paper: sea spray and changed turbulence structure during near-neutral stratification.

1) SEA SPRAY

Sea spray could possibly influence the exchange coefficients for both the latent and sensible heat. Breaking waves produce spray droplets that enhance the latent heat flux by allowing evaporation from the droplet surface. Evaporation in turn cools the air and thus enhances the sensible heat flux. Most measurements, however, do not distinguish between the spray-mediated fluxes and those originating directly from the sea surface. This makes analysis of the magnitude of the spray component difficult.

An indirect method is adopted in this study by running a flux model that takes account of spray effects (Andreas 2004, version 2.0). This model produces an approximate magnitude of the contribution of sea spray to the latent heat flux.

Basically, the Andreas model calculates the flux above the droplet evaporation layer, that is, what would be measured at about 10 m. This flux is considered to be a sum of the fluxes directly from the sea surface and the spray-mediated flux. The surface flux is calculated using the COARE 2.5 algorithm and the flux originating from sea spray is derived using a complex microphysical model.

The possible importance of sea spray was shown in Andreas and DeCosmo (2002) where Humidity Exchange over the Sea (HEXOS) data were used in the model (version 1.0). It was found that during wind speeds of about 10 m s^{-1} approximately 10% of the total latent heat flux originated from sea spray. For the wind speed range 15–18 m s^{-1}, the sea-spray-mediated flux accounted for as much as 10%–40% of the total flux.

2) THE TURBULENCE STRUCTURE

Smedman et al. (2007b) demonstrated that the ϕ function for heat decreased to zero during slightly unstable conditions close to neutral. This unexpected result was found to be related to a change of the turbulence structure that occurs for atmospheric conditions when $L \leq -150$ m. As the boundary layer approached neutral stratification, a high-frequency peak was observed to develop in $w\theta$ cospectra. In a transition regime, the cospectra had two peaks or a plateau form. The energy spectra of temperature were found to display a similar behavior. During these conditions, C_{HN} was observed to attain large numbers. Quadrant analysis showed that this was due to a top-down effect. Colder air from above entered the surface layer as downdrafts, increasing the flux of sensible heat. In Smedman et al. (2007b) this turbulence regime is referred to as the UVCN regime.

The neutral boundary layer was studied in Högström et al. (2002), where it was shown how detached eddies of surface-layer scale were created above the surface layer. As these detached eddies move downward and impinge on the surface, they are subject to blocking and are stretched out by the strong shear in the surface layer. Thus, the eddies become deformed, acquiring an along-wind length scale of several hundred meters but a vertical extent of approximately only 1/30 of the boundary layer height, that is, some tenths of meters [Fig. 1 in Högström et al. (2002) illustrates the principle underlying the process]. The high-frequency peak observed in the $w\theta$ cospectra and θ spectra for large $-L$ values is most likely a signature of such deformed eddies. Thus, the dry air, which was observed to enhance C_{HN} during near-neutral stratification, is likely to be transported to the surface by the detached eddies.

The unstable boundary layer during moderate winds is characterized by the horizontal roll type of eddy structure, a feature that has been both observed and modeled (e.g., Atlas et al. 1986; Mason and Sykes 1982). Smedman et al. (2007a) present a theory linking the horizontal rolls with the UVCN regime. As the thermal forcing of the boundary layer decreases, the large-scale eddy structure is bifurcated into one steady branch, the horizontal rolls, and one unsteady, the detached eddies. The likelihood of the formation of the detached eddies increases as the boundary layer approaches neutral stratification. Smedman et al. (2007a) speculated that h/L, where h is the height of the boundary layer, is the dominating quantity governing the development of the UVCN regime. However, in the absence of continuous measurements of the boundary layer height, L is used as the controlling parameter where $L < -150$ m is set as a limit when the UVCN regime appears. Smedman et al. (2007a) also show observations of the UVCN regime at a land site, which suggests that this is a dynamical process appearing independent of the nature of the surface, given the right atmospheric conditions.

3. Site and measurements

a. The site

The measurements were made at the Östergarnsholm Island, located at 57°27′N, 18°59′E in the Baltic Sea. This is a small flat island approximately 4 km east of the larger island of Gotland. Data were collected from a 30-m tower situated at the south end of the island. The site has been in semicontinuous use since 1995. A map can be found in Guo Larsén et al. (2004).

At 500 m from the coast of the island, the sea floor has approximately a 1:30 slope, and at a distance of 10 km the depth is approximately 50 m. A previous study (Smedman et al. 1999) concluded that measurements made at the site are indeed representative of deep-sea conditions for most situations. By calculating the flux footprint, Smedman et al. (1999) found that 90% of the turbulent fluxes measured at a height of 10 m originate from areas more than 250 m from the shoreline.

Smedman et al. (1999) also showed that the phase speed of the dominant waves varied between 92% and 99% of their deep-water values during low-wind conditions. During gale-force winds, some shallow-water effects could be seen in the phase speed of the dominant waves, varying between 77% and 94% of its deep-water value. However, no effects of shallow water on the turbulence structure were observed, even during gale-force winds.

In Smedman et al. (2003) it was demonstrated that under pure wind-sea conditions, the variation of the drag with wave age agrees very well with corresponding data from several deep-sea expeditions. These results strongly support the view that the measurements from the Östergarnsholm site indeed represent open-ocean conditions, at least for wind speeds up to 15 m s^{-1}.

Measurements of the water level at Visby Harbor, on the west coast of Gotland, provided by Swedish Meteorological and Hydrological Institute (SMHI) are used for calculation of the exact heights of the tower instrumentation. The variation of the water level is small, approximately ± 0.5 m, mainly due to the synoptic weather condition since tidal effects in the Baltic Sea are very small. The tower base is typically 1 m above the sea level.

b. Instrumentation

Measurements of turbulent fluctuations are made using Solent 1012R2 sonic anemometers (Gill Instruments, Lymington, United Kingdom) recording at 20 Hz at three levels on the tower (9, 16.5, and 25 m above the tower base), giving the flux of virtual sensible heat and momentum. Prior to installation, the sonic anemometers were calibrated individually in a wind tunnel, following a procedure similar to that described in Grelle and Lindroth (1994).

The sonic data have been corrected for errors originating from the cross-wind effect, according to Kaimal and Gaynor (1991). In addition, the sonic temperature flux has been corrected for influence from the latent heat flux (Schotanus et al. 1983).

Since November 2001, an LI-7500 open-path gas analyzer has been mounted at the 9-m level on the tower. Together with the sonic anemometer at this level, it gives the turbulent humidity flux as well as mean values of absolute humidity. The humidity flux has been corrected according to Webb et al. (1980). This correction is very small, amounting to a few percent at most.

Because of the separation distance (0.3 m) between the LI-7500 and the sonic anemometer the measured humidity flux is somewhat attenuated. We have adopted the Horst (2006) model to compensate for the flux loss. In mean, for the unstable cases studied in this paper, the correction is relatively small, about 2%.

To remove possible trends, a high-pass filter based on a 10-min running average was applied on the turbulence time series before variances and fluxes were calculated.

Slow-response sensors are placed at five levels on the tower (7, 11.5, 14, 20, and 28 m above the tower base), operating at 1 Hz, giving profile measurements of wind speed, wind direction, and temperature. Relative humidity is measured with a Rotronic instrument mounted 7 m above the tower base.

Water temperature measurements are made from a wave-rider buoy moored in 36-m-deep water, approximately 3.5 km southeast of Östergarnsholm (cf. Fig. 1), owned and operated by the Finnish Institute of Marine Research. The buoy measures the water temperature at a depth of 0.5 m, the bucket temperature, which is approximately equal to the skin temperature at this particular site (Rutgersson et al. 2001b).

In Smedman et al. (2007b), the ratio $\overline{w'\theta'}/U_{10}$ was plotted as a function of $\theta_w - \theta_{10}$. For unstable stratification the intercept of a first-order regression line with the x axis was 0.04 K. This result is taken as evidence that our measurements of $\theta_w - \theta_{10}$ are very close to the actual air–sea temperature difference under unstable conditions. Based on this result, we decided to retain data in cases in which the air–sea temperature difference is larger than 0.5 K (a similar analysis for stable stratification showed large scatter).

Since the instruments measuring the air and water temperatures are separated by 3.5 km, this good agreement is likely due to deep vertical mixing of the sea in combination with a positive heat flux. Such conditions dominate in the Baltic Sea in the autumn, the season

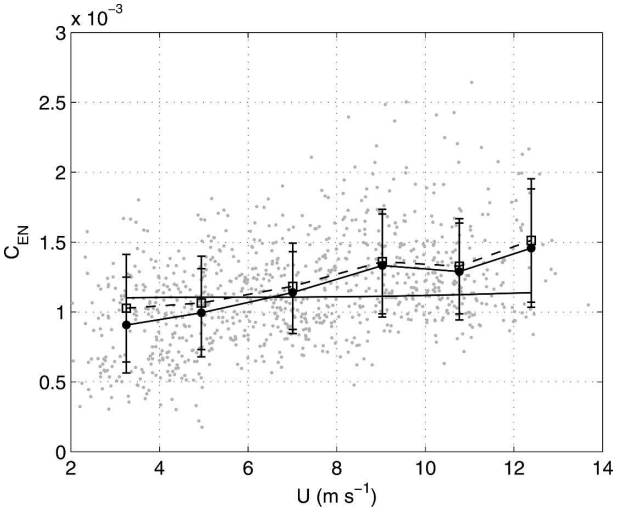

FIG. 1. The C_{EN} as a function of wind speed. Gray dots represent individual observations where C_{EN} has been calculated using the wave-dependent ϕ_m function. The solid line with filled circles represents the bin averages of these measurements with a bin size of 2 m s^{-1}. The dashed line with open squares represents bin-averaged values of C_{EN} calculated using a non-wave-dependent ϕ_m function. Error bars show ±1 std dev. Solid line without symbols represents C_{EN} calculated using the COARE 3.0 algorithm.

during which most of the data were collected. In addition, there is little incoming shortwave radiation in this season.

From Eq. (1a) an estimation of the mean percentage uncertainty of C_E is obtained through

$$\frac{\Delta C_E}{C_E} = \left\{ \left(\frac{\Delta \overline{w'q'}}{\overline{w'q'}} \right)^2 + \left(\frac{-\Delta U_{10}}{U_{10}} \right)^2 + \left[\frac{-\Delta (q_w - q_{10})}{(q_w - q_{10})} \right]^2 \right\}^{1/2}, \tag{12}$$

where Δ represents the uncertainty in each measurement. During May–June 2006, a second LI-7500 was mounted on the 10-m level for comparative flux measurements. Based on these results, the square root of the first right-hand-side term inside the square root was calculated to be 0.08. The mean value of U_{10} is 7 m s^{-1}, and ΔU_{10} is approximately 0.05 m s^{-1}, which makes $\Delta U_{10}/U_{10} \approx 0.01$. The uncertainty in the humidity gradient is mainly due to uncertainties in the water temperature measurements and the measurement of the relative humidity at 9 m. A value of 0.2 g kg^{-1} for $\Delta(q_w - q_{10})$ is reasonable. The mean value of the humidity gradient is 3 g kg^{-1}, which makes the square root of the last right-hand-side term inside the square root ≈ 0.07. By substituting these values into Eq. (12) the mean percentage uncertainty of C_E is calculated to 10%.

c. Data selection

Data have been selected according to the following six criteria: 1) wind was from the sea-fetch sector (50°–220°); 2) wind speed at 10 m was more than 2 m s^{-1}; 3) relative humidity was less than 95% (to avoid situations with condensation on the LI-7500 window); 4) there was approximate height constancy of $\overline{w'\theta'}$ and u_*; 5) the air–sea temperature difference was larger than 0.5 K and heat fluxes were positive, that is, there were unstable conditions; and 6) the air–sea specific humidity difference was larger than 1 g kg^{-1}. The dataset consists of 925 half-hour values. The mean ratio of u_* between 26 and 10 m is equal to 1.05, that is, a small systematic difference but completely acceptable. The majority of the data originate from the following periods: 2001–late October to early December, 2003–September and October, 2004–July and August, and 2005–July to early September.

4. Results

a. The neutral transfer coefficient and the roughness lengths, z_0 and z_{0q}

Figure 1 shows C_{EN} as a function of wind speed. The dots represents single 30-min values of C_{EN} calculated using the wave-dependent ϕ_m function, Eqs. (10a)–(10d). The solid line with filled circles represents bin averages of these data. The broken line with squares represents bin averages of C_{EN} calculated with a non-wave-dependent ϕ_m function, Eq. (11), and the solid line without symbols represents C_{EN} from the COARE 3.0 algorithm. The experimental data show a slight wind speed dependency for C_{EN} independent of the choice of ϕ_m function, whereas C_{EN} from the COARE algorithm is almost constant.

When introducing the wave-dependent nondimensional wind gradient, C_{EN} is reduced. However, C_{EN} is observed to have a larger reduction during low wind speeds, <7 m s^{-1}, compared to higher wind speeds. This is a result of swell being more frequent during low wind speeds. As an effect, C_{EN} displays a stronger wind speed dependency when the wave-dependent ϕ_m function is used.

In the mean, C_{EN} is reduced by 10% during swell, and 5% during mature sea when using the wave-dependent ϕ_m function. Whenever C_{EN} is shown in the following it has been calculated using the wave-dependent ϕ_m function.

The neutral transfer coefficient for humidity is shown as a function of the stability parameter, z/L, in Fig. 2. From this figure it appears that C_{EN} increases slightly as the atmosphere becomes more neutral. The scatter in-

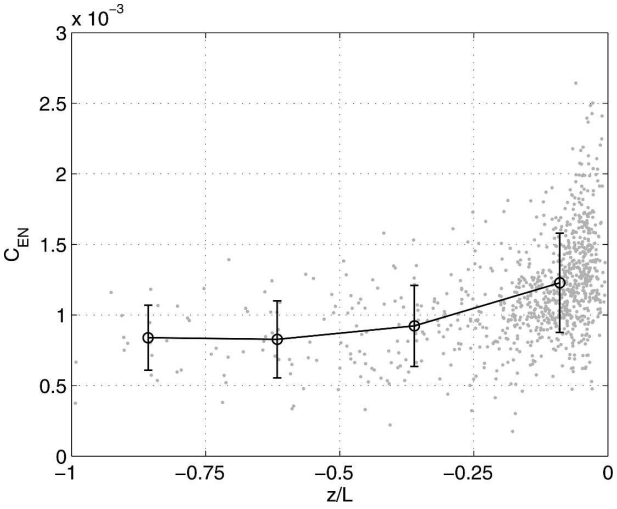

FIG. 2. The C_{EN} as a function of z/L. Dots = individual values of C_{EN}. Solid line = bin-averaged values over a z/L interval of 0.25. Error bars show ±1 std dev.

creases significantly and is very large as z/L approaches zero where the largest values of C_{EN} are observed.

In Fig. 3a C_{EN} is shown as a function of wind speed, but here the data are divided into three groups depending on the sea–air temperature difference. During periods with relatively large temperature differences, $\Delta T > 3$ K, C_{EN} is not clearly dependent on wind speed; a small decrease is even observed for $U > 7$ m s^{-1}. For $\Delta T < 2$ K the picture is completely different: C_{EN} increases continuously and is larger than the other groups at wind speeds greater than 9 m s^{-1}. Similar behavior is observed when the data are organized in terms of L (Fig. 3b): C_{EN} is found to increase with wind speed when $L < -150$ m. The COARE 3.0 parameterization seems to hold well for $\Delta T > 2$ K (or, in means of L, for $L > -150$ m).

Since the roughness lengths z_0 and z_{0q} determine C_{EN}, these parameters are analyzed in the same manner as C_{EN}. Figure 4 shows bin averages of z_0 as a function of wind speed. The data have again been organized into three groups representing different ΔT values. Also shown is z_0 calculated with the COARE 3.0 algorithm (solid line). From this figure it is clear that the measured z_0 seem to have the same wind speed dependence as the COARE 3.0 parameterization and is independent of the sea–air temperature difference. This is expected, since physically there is no reason why z_0 should be related to temperature. A similar result is found when organizing data in terms of L (not shown). Thus, variation (or lack of variation) in z_0 cannot explain the observed variation of C_{EN} shown in Figs. 3a and 3b.

Figure 5 shows bin-averaged values of z_{0q} as a function of wind speed, divided into three groups depending on the value of ΔT. The solid line represents z_{0q} from COARE 3.0, which is seen to decrease with increasing wind speed, as does the curve representing conditions with $\Delta T > 3$ K. However, for data representing smaller ΔT, z_{0q} is seen to increase with wind speed for $U > 10$ m s^{-1}. The group containing the smallest sea–air temperature differences displays the largest increase. As seen from Eq. (8a), this increase in z_{0q} implies a corresponding increase in C_{EN}, which was observed in Figs. 3a and 3b.

Figure 6 depicts the dependence of C_{EN} on both temperature difference and wind speed. The data have been divided into three groups depending on wind speed and are shown as a function of ΔT. For wind

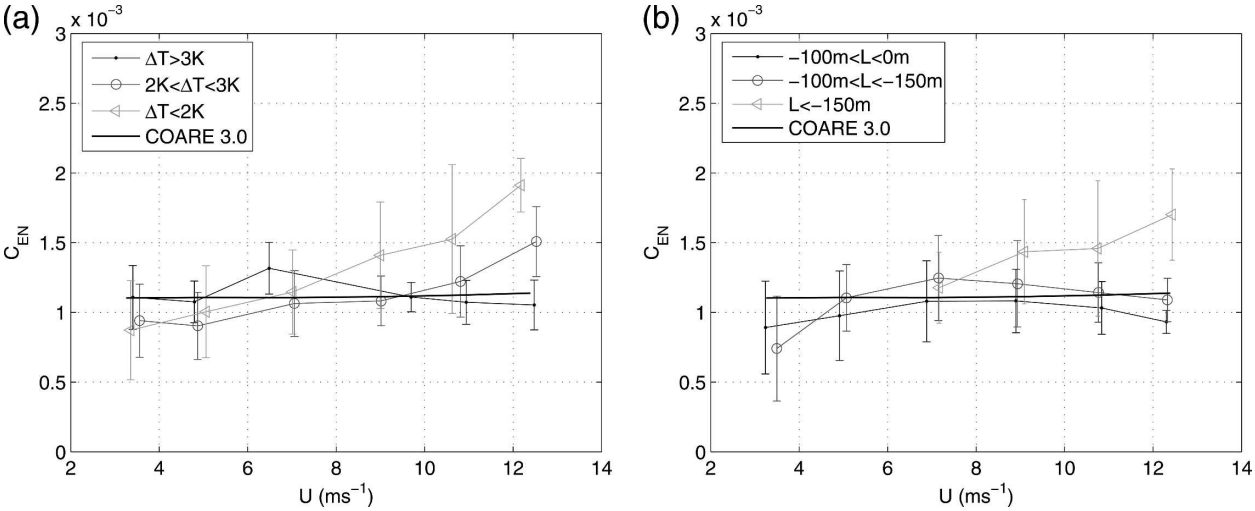

FIG. 3. (a) Bin-averaged values of C_{EN} as a function of wind speed. Data are divided by ΔT; symbols are defined in the legend. (b) Bin-averaged values of C_{EN} as a function of wind speed. Data are divided by L; symbols are defined in the legend.

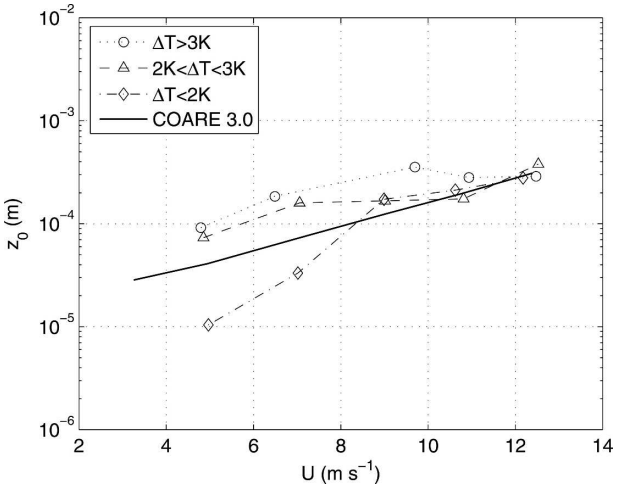

FIG. 4. Bin-averaged values of z_0 as a function of wind speed. Symbols are defined in legend.

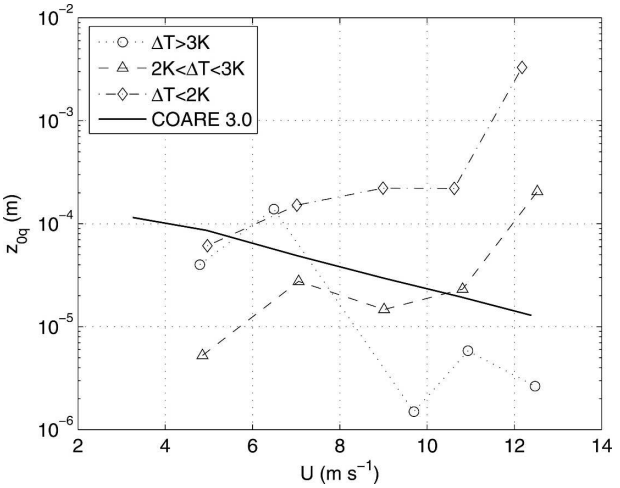

FIG. 5. Bin-averaged values of z_{0q} as a function of wind speed. Symbols are defined in legend.

speeds below 8 m s^{-1} (Fig. 6a) no dependence on ΔT is found; C_{EN} is constant, with a value of 1.01×10^{-3}, as indicated by the solid line. This is not the case for higher wind speeds; for $9 < U < 12$ m s^{-1} (Fig. 6b), C_{EN} is seen to increase with decreasing ΔT. The solid line shows a linear fit, which can be used for prediction of C_{EN} during conditions with a ΔT of 0.5–5 K using the equation $10^3 C_{\mathrm{EN}} = -0.14\Delta T + 1.56$. An even stronger dependence on ΔT is found for wind speeds above 12 m s^{-1}, as shown in Fig. 6c. For this group, a tentative quadratic fit is suggested for $\Delta T < 5$ K, with the equation $10^3 C_{\mathrm{EN}} = 0.115\Delta T^2 - 1.06\Delta T + 3.39$.

The trends of these regression lines are consistent with those presented for C_{HN} in Smedman et al. (2007b), indicating a similar process influencing both the sensible and latent heat flux during conditions of small air–sea temperature difference and high wind speeds.

In Fig. 7 the latent heat flux calculated with the COARE 3.0 algorithm is compared with the measured flux. COARE 3.0 approximately follows the measurements at small fluxes although there is a slight overestimation for measured fluxes smaller than about 70 W m^{-2}. This is probably due to the presence of longer waves, which decrease the C_{EN} value through the ϕ_m function, a feature that is not implemented in the COARE 3.0 algorithm. For measured fluxes larger than 80 W m^{-2} there is systematic underestimation by COARE amounting to approximately 30 W m^{-2} at a measured latent heat flux of 180 W m^{-2}. This is a consequence of the results presented in Figs. 3a and 3b, where the observed C_{EN} at small ΔT and high wind speeds are seen to deviate from the C_{EN} suggested by the COARE 3.0 algorithm.

b. Cospectral analysis

To understand the physical processes that govern the air–sea exchange of latent heat, spectral analysis was performed. The data have been divided into nine groups depending on wind speed and air–sea temperature difference (see Table 1). Table 1 also shows the number of entries in each group, the mean value of the Obukhov length (L), and the mean C_{EN} value. The highest C_{EN} values are found in group 9, where ΔT is less than 2 K, the wind speed exceeds 10 m s^{-1}, and $-L$ is large. Median values of cospectra for each group have been calculated from the 30-min time series of 20-Hz data.

In Fig. 8, the normalized cospectra of vertical velocity and specific humidity, nC_{wq}, are shown as a function of normalized frequency, $f = nz/U$, in a linear–logarithmic representation, where n = frequency. Note that this representation is area preserving, the area enclosed by the curve being proportional to the total covariance. The columns in Fig. 8 represent different ranges of air–sea temperature differences; the rows represent different ranges of wind speed. Cospectra are normalized with the flux itself; thus, integration of the normalized cospectra equals unity.

A striking feature of Fig. 8 is revealed by dividing the cospectra as per Table 1, that is, into different groups depending on the values of ΔT and U. As the wind speed increases and the air–sea temperature difference decreases, a secondary peak develops in the high-frequency range. That is, the high-frequency maximum increases both downward and to the right in the figure. In the subfigure representing cases where $U > 10$ m s^{-1} and $\Delta T < 2$ K (group 9), the low-frequency peak has

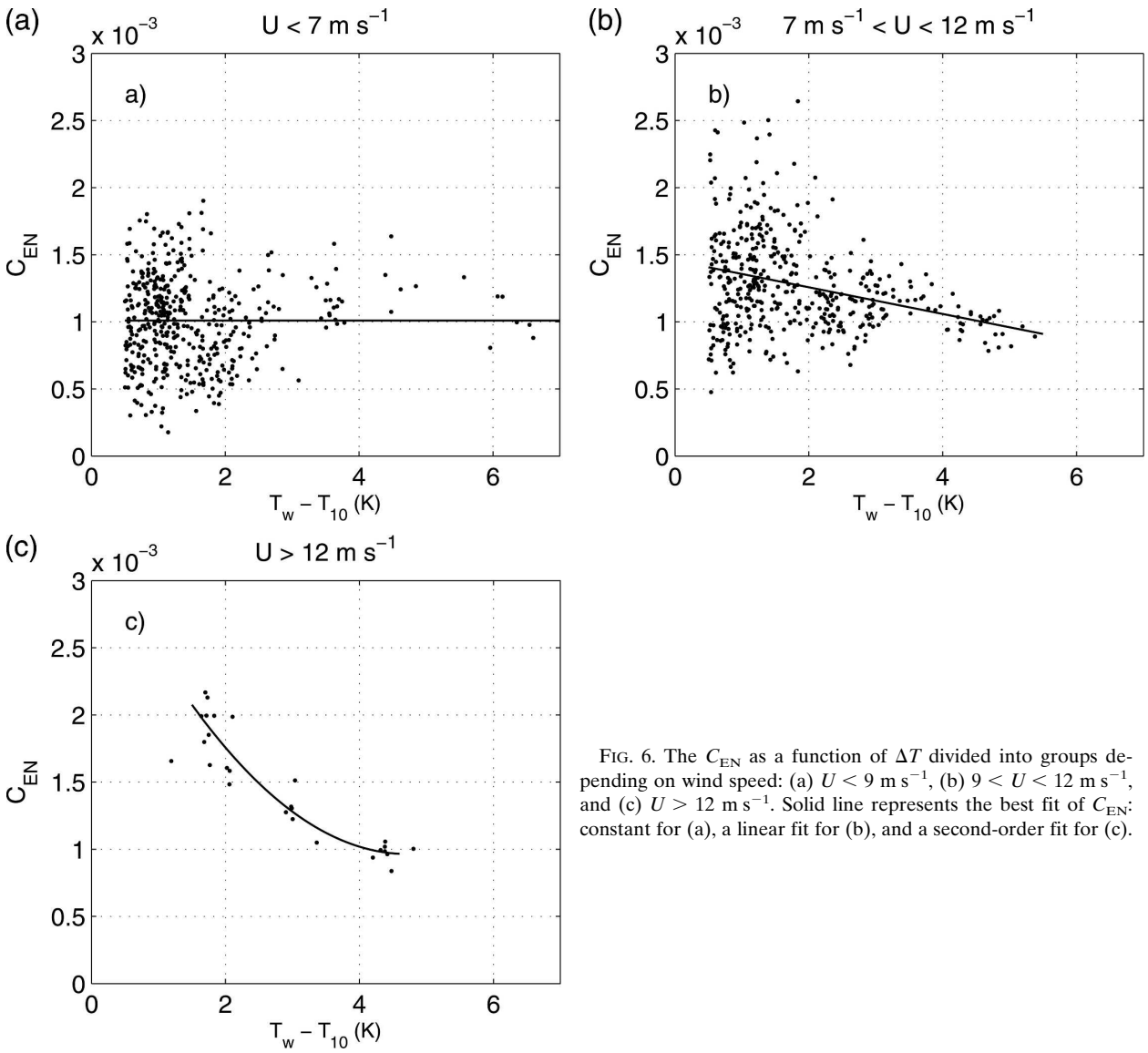

FIG. 6. The C_{EN} as a function of ΔT divided into groups depending on wind speed: (a) $U < 9$ m s^{-1}, (b) $9 < U < 12$ m s^{-1}, and (c) $U > 12$ m s^{-1}. Solid line represents the best fit of C_{EN}: constant for (a), a linear fit for (b), and a second-order fit for (c).

almost disappeared. This means that the vertical turbulent flux of specific humidity is dominated by relatively small scale eddies. As seen in Table 1, this group displays the largest C_{EN} values.

Double-peaked cospectra have previously been observed in the marine boundary layer. Smith and Anderson (1984) measured turbulence at Sable Island, Nova Scotia, Canada, and presented evidence of a double structure in the near-neutral cospectra of both humidity and temperature flux. They describe these cospectra as being camel shaped but make no further comments about them.

Schmitt et al. (1979) report saddle-shaped cospectra of wq and $w\theta$, but offer no explanation for them. The same saddle shape is found by Sempreviva and Gryning (1996) in their normalized cospectra of wq, measured in the sound between Denmark and Sweden. The two peaks they found are not as pronounced as those examined in this study, but this is probably related to their choice of log–log representation.

Phelps and Pond (1971) present cospectra of $w\theta$, calculated from measurements made on the R/P *Floating Instrument Platform* (*FLIP*) in the Barbados Oceanographic and Meteorological Experiment (BOMEX). These cospectra have a high-frequency peak only, very similar to the group representing the smallest ΔT and largest wind speeds in Fig. 9. Phelps and Pond (1971) also present cospectra measured on a pre-BOMEX trial cruise outside San Diego, California, that have only a low-frequency peak. The difference between these two

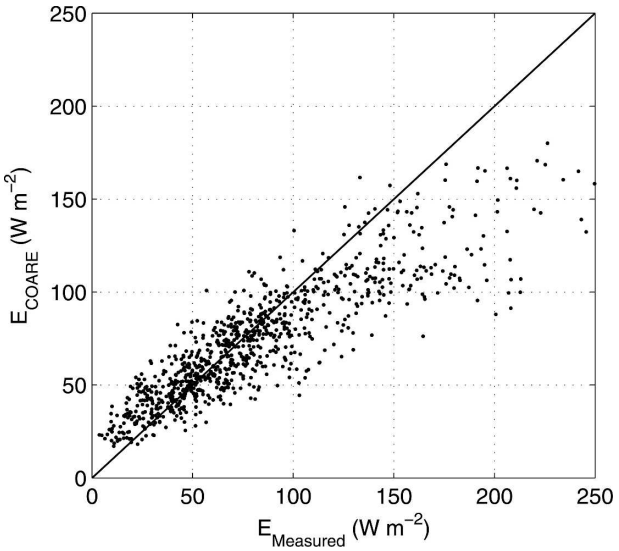

FIG. 7. Comparison of measured latent heat flux with the flux calculated with the COARE 3.0 algorithm. Solid straight line represents the 1:1 ratio.

measurements is the air–sea temperature difference. The ΔT of the data collected outside San Diego was approximately 3 K, whereas the BOMEX measurements were made under conditions in which the ΔT was as low as 0.5 K. These results agree with ours.

Cospectra presented in Fig. 8 closely resemble those obtained for $w\theta$ using the very accurate Meteorological Institute of the University of Uppsala turbulence instrument during a 1999 measurement campaign (Smedman et al. 2007b) for corresponding combinations of ΔT and U.

c. Quadrant analysis

Quadrant analysis is a conditional sampling technique originally developed for use with turbulent laboratory flows by Lu and Willmarth (1973). It separates the flux into four categories, according to the signs of the two fluctuating components. Thus, using two components denoted x and y and numbering the quadrants according to mathematical convention, we have the following quadrants for the x–y plane: quadrant I: $x > 0$ and $y > 0$, quadrant II: $x < 0$ and $y > 0$, quadrant III: $x < 0$ and $y < 0$, and quadrant IV: $x > 0$ and $y < 0$, where $y = w$ and $x = q$ in our case. Positive contributions to the specific humidity flux are obtained from quadrant I, humid air being transported upward (bursts or ejections), and quadrant III, dry air moving downward (sweeps or gusts). Negative contributions are obtained from quadrants II and IV.

The importance of relatively short-lived large values of the $x'y'$ moments may be seen by estimating the contribution of these events to the total flux, and by comparing the result with the proportion of time these large values occur. This is accomplished by determining the cumulative frequency distributions of the fluxes when keeping values larger than a given fraction of the average flux. This is equivalent to using the hyperbolic hole introduced by Willmarth and Lu (1974). The size H of the hole is defined as

$$H = |x'y'|/\overline{|x'y'|}, \tag{13}$$

where the point (x', y') lies on the hyperbola that bounds the hole region in the x–y plane. The hyperbolic hole is defined as the shaded area in Fig. 9 and is a region excluded from the quadrant analysis; that is, data *outside* the hole are kept for the analysis. By progressively increasing the magnitude of H, the importance of events exhibiting increasingly large values of $|x'y'|$ can be determined in each quadrant.

Following Raupach (1981), a flux fraction, S_{iH} (with subscript i referring to the quadrant number) is defined as

$$S_{iH} = [x'y']_{iH}/\overline{x'y'}, \tag{14}$$

where the brackets signify a conditional average. This conditional average is formally defined using a conditioning function I_{iH} that obeys $I_{iH} = 1$ if the point lies in the ith quadrant and $|x'y'| \geq H\overline{|x'y'|} = 0$ otherwise.

Then the conditionally averaged flux becomes

$$[x'y']_{iH} = \lim \inf \frac{1}{T} \int_0^T x'y'(t) I_{iH}(t)\, dt. \tag{15}$$

Since the flux fractions are normalized quantities, it is clear that

$$\sum_{i=1}^{4} S_{i,0} = 1. \tag{16}$$

Figures 10a and 10b present quadrant analyses of two cases with different values of L. These cases are typical of situations in which $L > -150$ m and $L < -150$ m, respectively. Note that the parameters presented in

TABLE 1. Description of the groups used in the spectral analysis.

Group	$\Delta T = T_w - T_{10}$ (K)	U (m s^{-1})	Entries	Mean L (m)	Mean $C_{EN} \times 10^3$
1	$\Delta T > 3$	$U < 5$	21	−26	1.11
2	$\Delta T > 3$	$5 < U < 10$	19	−71	1.16
3	$\Delta T > 3$	$U > 10$	57	−114	1.07
4	$2 < \Delta T < 3$	$U < 5$	32	−32	1.02
5	$2 < \Delta T < 3$	$5 < U < 10$	73	−81	1.04
6	$2 < \Delta T < 3$	$U > 10$	52	−187	1.26
7	$\Delta T < 2$	$U < 5$	196	−44	0.87
8	$\Delta T < 2$	$5 < U < 10$	397	−166	1.24
9	$\Delta T < 2$	$U > 10$	78	−403	1.57

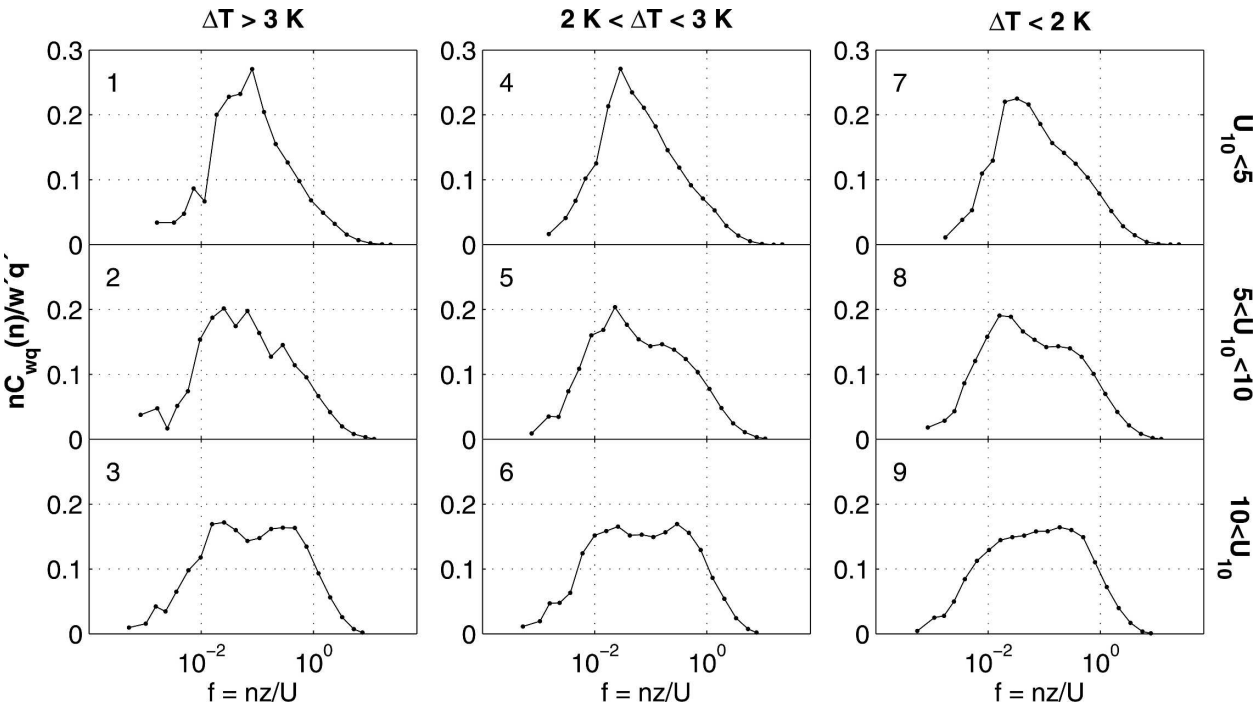

FIG. 8. Normalized cospectra for vertical wind and specific humidity, divided according to wind speed (rows) and ΔT (columns). Numbers in the upper-left corner of each panel refer to the groups in Table 2.

these figures differ from those in Fig. 9: Fig. 9 has w' and q' on the axes, whereas Fig. 10 has hole size and the humidity flux fraction on the corresponding axes.

Figure 10a represents a moderately unstable case in which $L = -33$ m and $C_{EN} = 1.06 \times 10^{-3}$. The quadrant analysis of this case reveals that the humidity flux is largely dominated by quadrant I, that is, humid air moving upward, as intuitively expected.

Figure 10b represents a case in which the stability is very close to neutral, $L = -280$ m and $C_{EN} = 1.60 \times 10^{-3}$. The quadrant analysis of this case reveals a very different situation from that depicted in Fig. 10a. The contributions to the flux from quadrant III have increased significantly, which suggests that the observed increase in C_{EN} for large negative values of L is connected to an enhancement of the flux due to downward-moving, dry air.

Tables 2a and 2b show the contributions from each quadrant for hole sizes 0, 3, 6, and 9; that is, this table put numbers to Figs. 10a and 10b. Note that the sum of all quadrants in both cases is equal to 1 for hole size 0, as stated by Eq. (16). As in Fig. 10, Table 2 points to a situation in which the turbulent humidity flux during the neutral case to a greater extent is dominated by large events of downward-moving dry air than in the unstable case. For instance, considering hole size 6 for the near-neutral case (Table 2b) the sum of all quadrants equals 0.40; that is, 40% of the net flux occurs in events that are 6times the mean flux. The absolute sum of all quadrants, that is, $\Sigma_{i=1}^{4}|S_{i,6}|$, is equal to 0.58. This sum can be interpreted as the flux turnover, that is, a measure of the activity in events (positive and negative)

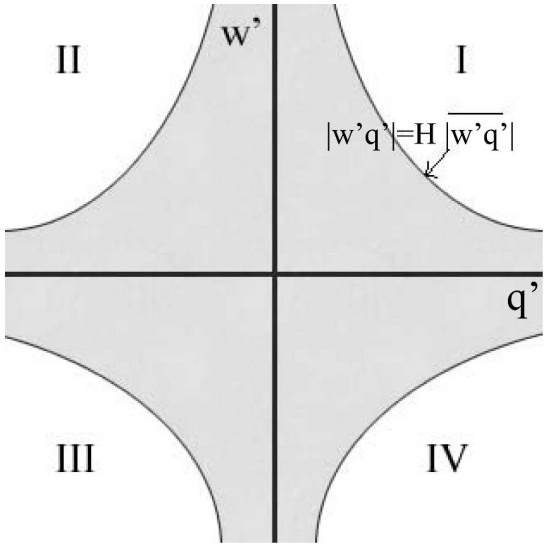

FIG. 9. Specific humidity and vertical velocity fluctuation domain, showing the quadrants and the hyperbolic excluded region (shaded area); H is size of the hyperbolic hole.

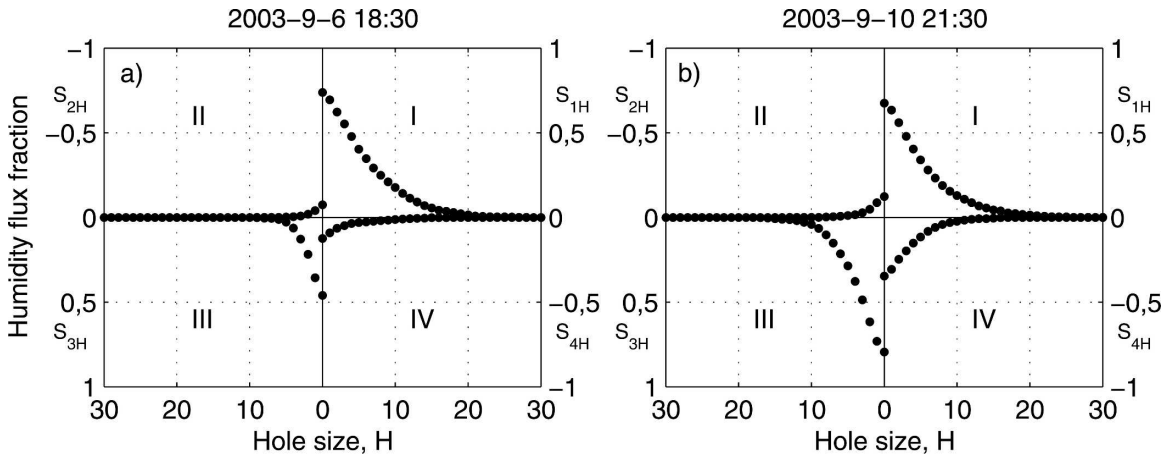

FIG. 10. Examples of quadrant analysis. (a) A case in which $L = -33$ m, and (b) a case that is very close to neutral in which $L = -280$ m. The figures give the flux fraction for each quadrant as a function of hole size. Note that the hole size by definition is always positive. Positive contributions to the latent heat flux are provided by quadrants I and III, and negative contributions are provided by quadrants II and IV.

that are 6 times the net flux. Out of this, 0.21/0.58 = 36% occurs in downburst (sweeps) of dry air. A similar exercise for the unstable case (Table 2a) yields the following result: 33% of the net flux occurs in events that are 6 times the mean flux; the flux turnover $\Sigma_{i=1}^{4}|S_{i,6}|$ is equal to 0.39, that is, less activity in large events than in the near-neutral case. The relative contribution by downburst (quadrant III) to events of hole size 6 is only 0.01/0.39 $\approx$ 2.5% for the unstable case.

d. Modeled sea spray

The effect of sea spray is investigated (see Table 3) using the model described in Andreas (2004). To relate this analysis to previously presented results, the data are divided into groups depending on wind speed and air–sea temperature difference.

Table 3a presents the number of data in each group, and Table 3b shows the mean value of C_{EN}. The value at $U < 7$ m s^{-1} is used as a reference in Table 3c to calculate the percentage increase of C_{EN} for groups with higher wind speed. Table 3d shows the relative contribution of sea spray to the total latent heat flux as calculated by the model.

By comparingTables 3c and 3d, that is, by comparing the actual increase in C_{EN} to the expected increase due to sea spray according to the model, the conclusion is made that although sea spray contributes somewhat to the total flux, it cannot alone explain the whole increase in C_{EN}. This is seen by examining the group with the highest wind speed and smallest ΔT; this group displays

TABLE 2. Results from quadrant analysis, giving magnitude of the different quadrants in two cases for four hole sizes.

Hole size	Quadrants I	II	III	IV
(a) $L = -33$ m (1830 LST 6 Sep 2003)				
0	0.74	−0.08	0.46	−0.12
3	0.55	−0.01	0.13	−0.05
6	0.35	0.00	0.01	−0.03
9	0.21	0.00	0.00	−0.02
(b) $L = -280$ m (2130 LST 21 Oct 2003)				
0	0.68	−0.12	0.80	−0.36
3	0.48	−0.03	0.49	−0.20
6	0.28	−0.01	0.21	−0.08
9	0.15	0.00	0.07	−0.03

TABLE 3. Investigation of the influence of sea spray on C_{EN} based on the model by Andreas (2004). (a) The number of members in each group, (b) the mean value of C_{EN}, (c) the percentage increase in C_{EN} with wind speed when using the groups for which $U < 7$ m s^{-1} as a reference (Ref), and (d) the contribution of sea spray to the total flux according to the model.

	Wind speed interval	$\Delta T >$ 3 K	$2 < \Delta T <$ 3 K	$\Delta T <$ 2 K
(a) Entries	$U < 7$	31	53	369
	$7 < U < 10$	9	52	224
	$U > 10$	57	52	78
(b) $C_{EN} \times 10^3$	$U < 7$	1.12	0.97	0.98
	$7 < U < 10$	1.09	1.06	1.28
	$U > 10$	1.05	1.24	1.53
(c) Increase	$U < 7$	Ref	Ref	Ref
	$7 < U < 10$	−2.5%	9.3%	30.5%
	$U > 10$	−6%	27%	56.3%
(d) Spray flux	$U < 7$	0.2%	0.6%	0.7%
	$7 < U < 10$	4.5%	4.3%	4.2%
	$U > 10$	6.2%	10%	9.9%

an increase of about 56% in C_{EN}, but the contribution of sea spray to the total flux is about 10%.

The magnitude of the spray-mediated portion of the total latent heat flux is of approximately the same magnitude as that found in Andreas and DeCosmo (2002), where the influence of sea spray on the HEXOS data was examined.

5. Discussion

Table 4 summarizes some well-known studies of C_{EN}, including information about the instrumentation and method used to derive the humidity flux measured using either the eddy correlation method (EC) or the inertial dissipation method (ID). Since the increase in C_{EN} is found for small values of ΔT, a column is included to show whether small ΔT values were excluded. The last three columns show the wind speed range in which the measurements were made, the mean C_{EN} value, and whether any dependence on wind speed was found.

The mean values of C_{EN} presented in Table 4 range from $1.10 \times 10^{-3} \pm 0.22 \times 10^{-3}$ to $1.5 \times 10^{-3} \pm 0.5 \times 10^{-3}$. Using the wave-dependent ϕ_m functions, the mean C_{EN} value for this study is $1.15 \times 10^{-3} \pm 0.37 \times 10^{-3}$ ($1.20 \times 10^{-3} \pm 0.37 \times 10^{-3}$ using the non-wave-dependent ϕ_m function); that is, considering only the mean value, this is in general agreement with previous field experiments. The standard deviation is quite large, larger than most of the standard deviations presented in Table 4. Measurement uncertainty justifies a scatter of approximately 10% (i.e., $\pm 0.1 \times 10^{-3}$), as discussed in section 3b. Remaining scatter must be explained by physical processes influencing the air–sea humidity exchange.

The wind speed dependency shown in Fig. 1 is supported by some of the previous investigations. As shown in Fig. 3a, this effect is most evident for situations with $\Delta T < 2$ K. None of the studies presented in Table 4 divided the data into groups depending on air–sea temperature differences. Had such an analysis been done, a clearer dependence on wind speed might have emerged. However, this requires an extensive dataset, covering a wide range of wind speed and ΔT measurements, which might not be available for experiments conducted during a limited period of time.

Surface renewal theory is unable to predict the observed high C_{EN} values. Two possible explanations were presented in section 2d. In theory, wave breaking could also be a plausible explanation. As waves break they disturb the interfacial, diffusive sublayer, thus reducing the resistance of this bottleneck layer and making the transfer of latent heat more efficient. During

TABLE 4. Summary of some well-known field experiments (prop anem = propeller-vane anemometer). Here, AMTEX is the Airmass Transformation Experiment, TOSCANE is the Travaux d'Océanographie Spatiale Capteurs Actifs Atlantique Nord Est, CATCH is Couplage avec l'Atmosphère en Conditions Hivernale, and FETCH is Flux, Etat de la Mer, et Télédétection en Conditions du Fetch Variable.

Reference	Dataset	Instrumentation	Method	ΔT criterion (K)	U range ($m\ s^{-1}$)	Mean C_{EN} ($\times 10^3$)	C_{EN} U trend
Francey and Garratt (1978)	AMTEX (tower)	Prop anem + IR hygrometer	EC	>4.5	5–13	1.5 ± 0.3	Possible (75% confidence)
Anderson and Smith (1981)	Sable Island (tower)	PAT311-1 sonic + Lyman α	EC	None, ΔT range: 0.2–3.1	5–12	1.27 ± 0.26	Clear
Large and Pond (1982)	Ships	Prop anem + Lyman α	ID	>1	4–14	1.15 ± 0.22	Weak
Saïd and Druilhet (1991)	TOSCANE-T (airborne measurements)	Pitot probe + Lyman α	EC	None, ΔT range: 1–2	1–15	1.6	None (for $U < 12\ m\ s^{-1}$)
DeCosmo et al. (1996)	HEXOS (North Sea platform)	Prop anem + Lyman α	EC	>1.5	6–18	1.12 ± 0.24	None
Eymard et al. (1999)	CATCH (ship)	Prop anem + Refractometer	ID	No information	5–20	1.13 (for $U < 6.5\ m\ s^{-1}$)	Clear, for $U > 6.5\ m\ s^{-1}$
Oost et al. (2000)	North Sea platform	Solent R2A + Lyman α and IFM	EC	>0.8	2–18	1.10 ± 0.22	None
Pedreros et al. (2003)	FETCH (ship)	Solent R3HS + prop anem + refractometer	EC+ID	None	2–19	1.23 ± 0.24 (EC)	In ID

such conditions, application of surface renewal theory is questionable. However, as illustrated by Figs. 3a and 3b, high wind speeds are not enough to explain the high C_{EN} values found. A combination of relatively high wind speeds with a small temperature difference is needed. Thus wave breaking is probably not the primary reason for the observed increase in C_{EN}.

Spectra and quadrant analyses indicate that the high C_{EN} values are connected to a change in the turbulence structure. This result is analogous to what was observed for C_{HN} in Smedman et al. (2007b) during the UVCN regime, presented in section 2d(2). The high-frequency peak in the wq cospectra, which develops as the wind speed increases and ΔT decreases, as shown in Fig. 8, was also observed for the $w\theta$ cospectra in Smedman et al. (2007b). This peak is probably a signature of the detached eddies, which are created in the UVCN regime.

According to the quadrant analysis (Fig. 10b), dry air from above is brought down to the surface in the near-neutral case. In the framework of the UVCN theory, this transport is governed by the detached eddies. As an effect, the humidity flux is enhanced, which would explain the large C_{EN} values observed during high wind speeds and small air–sea temperature differences. Similarly, Smedman et al. (2007b) show that the large C_{HN} observed during near-neutral conditions are connected to events with downward transport of cold air.

These results agree very well with those presented in Maitani and Ohtaki (1989). From measurements made above a paddy field they showed that downdrafts were more efficient in the upward transport of humidity during near-neutral stratification.

A peculiar discrepancy between the behavior of C_{EN} and of C_{HN} becomes evident when the results of Smedman et al. (2007b) are compared with those of the present study. The increase in C_{EN} with wind speed appears only during conditions of small sea–air temperature differences. However, C_{HN} is observed to increase with wind speed independent of the magnitude of ΔT; albeit the largest increase is observed to occur with the largest negative values of L.

6. Summary and conclusions

The vertical turbulent transport of latent heat in the marine surface layer was studied using a Licor-7500 open-path gas analyzer in combination with a sonic anemometer. The focus was to study the neutral exchange coefficient C_{EN}. It was found that the exchange coefficient increases systematically as the air–sea temperature difference decreases and the wind speed increases. Using the Andreas (2004) flux model, which incorporates the effects of sea spray, the conclusion is made that sea spray is not the major reason for the observed increase in C_{EN}.

The high C_{EN} values are observed during situations when there is a regime shift of the structure of the turbulence. From spectral analysis it was found that as the boundary layer approaches neutral stratification, smaller-scale eddies become increasingly important in the turbulent transport of humidity. Quadrant analysis showed that the smaller-scale eddies were connected to situations with strong downdrafts of dry air, which would explain the enhancement of C_{EN}.

These findings were found to be analogous to the results concerning the exchange of sensible heat presented in Smedman et al. (2007b). Similar enhancement of the exchange coefficient C_{HN} was reported during near-neutral stratification in combination with a high-frequency peak in the $w\theta$ cospectra and downdrafts of colder air. This special regime of the turbulence structure was termed the unstable very close to neutral regime and it is treated thoroughly in Smedman et al. (2007a).

In summary, the UVCN regime develops in moderate to strong winds as the thermal forcing of the boundary layer decreases. It is described as the unstable branch of the larger-scale eddy structure, where the steady branch consists of the well-known horizontal rolls. During the UVCN regime, eddies with a vertical extent of approximately surface-layer height dominate the turbulent transport. These eddies originate as detached eddies above the surface layer and move toward the surface, bringing down drier, colder air, enhancing the surface fluxes of sensible and latent heat.

The wave-dependent ϕ_m functions from Guo Larsén et al. (2004) were applied when calculating C_{EN}. It was found that this had the effect of reducing the exchange coefficient. In the mean the reduction was about 10% during swell and 5% during mature sea. This reduction will act to enlarge the wind speed dependency of C_{EN} since swell is mainly prevalent during lower wind speeds. However, the wave-dependent, nondimensional profile function for wind was derived for wind following swell. Its applicability for other conditions, such as multidirectional swell or cross swell, is not known.

A comparison with the COARE 3.0 flux algorithm was made, and it was found that it holds well during conditions when the air–sea temperature difference is more than 3 K. However, for smaller temperature differences and wind speeds above about 8 m s^{-1} the algorithm underestimates the exchange coefficient as a result of the formation of the UVCN regime, an effect that is not implemented in the algorithm.

Acknowledgments. The authors are grateful to Drs. H. Bergström and C. Johansson for valuable help with the meteorological measurements. We thank Drs. K. Kahma and H. Pettersson who provided the wave measurements and water temperature data. We acknowledge Edgar Andreas for allowing us to use his model, Maria Norman for the results from the LI-7500 comparison test, and Barry Broman at SMHI for providing water level data at Visby Harbor. The work was sponsored by the Swedish Research Council under Contract 621-2002-5348.

REFERENCES

Anderson, R. J., and S. D. Smith, 1981: Evaporation coefficient for the sea surface from eddy flux measurements. *J. Geophys. Res.,* **86,** 449–456.

Andreas, E. L, 2004: A bulk air-sea flux algorithm for high-hind, spray conditions, version 2.0. Preprints, *13th Conf. on Interactions of the Sea and Atmosphere,* Portland, ME, Amer. Meteor. Soc., P1.5.

——, and J. DeCosmo, 2002: The signature of sea spray in the HEXOS turbulent heat flux data. *Bound.-Layer Meteor.,* **103,** 303–333.

Atlas, D., B. Walter, S.-H. Chou, and P. J. Sheu, 1986: The structure of the unstable marine boundary layer viewed by lidar and aircraft observations. *J. Atmos. Sci.,* **43,** 1301–1318.

Brutsaert, W., 1975: A theory for evaporation (or heat transfer) from rough and smooth surfaces at ground level. *Water Resour. Res.,* **11,** 543–550.

Clayson, C. A., C. W. Fairall, and J. A. Curry, 1996: Evaluation of turbulent fluxes at the ocean surface using surface renewal theory. *J. Geophys. Res.,* **101,** 28 503–28 513.

DeCosmo, J., K. B. Katsaros, S. D. Smith, R. J. Anderson, W. A. Oost, K. Bumke, and H. Chadwick, 1996: Air-sea exchange of water vapor and sensible heat: The Humidity Exchange over the Sea (HEXOS) results. *J. Geophys. Res.,* **101,** 12 001–12 016.

Edson J. B., C. J. Zappa, J. A. Ware, W. R. McGillis, and J. E. Hare, 2004: Scalar flux profile relationships over the open ocean. *J. Geophys. Res.,* **109,** C08S09, doi:10.1029/2003JC001960.

Eymard, L., and Coauthors, 1999: Surface fluxes in the North Atlantic current during CATCH/FASTEX. *Quart. J. Roy. Meteor. Soc.,* **125,** 3563–3599.

Fairall, C. W., E. F. Bradley, D. P. Rogers, J. B. Edson, and G. S. Young, 1996: Bulk parameterization of air-sea fluxes for Tropical Ocean–Global Atmosphere Coupled Ocean–Atmosphere Response Experiment. *J. Geophys. Res.,* **101,** 3747–3764.

——, ——, J. E. Hare, A. A. Grachev, and J. B. Edson, 2003: Bulk parameterization of air–sea fluxes: Updates and verification for the COARE algorithm. *J. Climate,* **16,** 571–591.

Francey, R. J., and J. R. Garratt, 1978: Eddy flux measurements over the ocean and related transfer coefficients. *Bound.-Layer Meteor.,* **14,** 153–166.

Grelle, A., and A. Lindroth, 1994: Flow distortion by a Solent sonic anemometer: Wind tunnel calibration and its assessment for flux measurements over forest and field. *J. Atmos. Oceanic Technol.,* **11,** 1529–1542.

Guo Larsén, X., A. Smedman, and U. Högström, 2004: Air–sea exchange of sensible heat over the Baltic Sea. *Quart. J. Roy. Meteor. Soc.,* **130,** 519–539.

Högström, U., 1988: Non-dimensional wind and temperature profiles in the atmospheric surface layer: A re-evaluation. *Bound.-Layer Meteor.,* **42,** 55–78.

——, 1996: Review of some basic characteristics of the atmospheric surface layer. *Bound.-Layer Meteor.,* **78,** 215–246.

——, J. C. R. Hunt, and A. Smedman, 2002: Theory and measurements for turbulence spectra and variances in the atmospheric neutral surface layer. *Bound.-Layer Meteor.,* **103,** 101–124.

Horst, T. W., 2006: Attenuation of scalar fluxes measured with horizontally-displaced sensors. Preprints, *17th Symp. on Boundary Layers and Turbulence,* San Diego, CA, Amer. Meteor. Soc., 7.5.

Kaimal, J. C., and J. E. Gaynor, 1991: Another look at sonic thermometry. *Bound.-Layer Meteor.,* **56,** 401–410.

Large, W. G., and S. Pond, 1982: Sensible and latent heat flux measurements over the ocean. *J. Phys. Oceanogr.,* **12,** 464–482.

Liu, W. T., K. B. Katsaros, and J. A. Businger, 1979: Bulk parameterization of air-sea exchanges of heat and water vapor including the molecular constraints at the interface. *J. Atmos. Sci.,* **36,** 1722–1735.

Lu, S. S., and W. W. Willmarth, 1973: Measurements of the structure of the Reynolds stress in a turbulent boundary layer. *J. Fluid Mech.,* **60,** 481–511.

Maitani, T., and E. Ohtaki, 1989: Turbulent transport processes of carbon dioxide and water vapor in the surface layer over a paddy field. *J. Meteor. Soc. Japan,* **67,** 809–815.

Mason, P. J., and R. I. Sykes, 1982: A two-dimensional numerical study of horizontal roll vortices in an inversion capped planetary boundary layer. *Quart. J. Roy. Meteor. Soc.,* **108,** 801–823.

Oost, W. A., C. M. J. Jacobs, and C. van Oort, 2000: Stability effects on heat and moisture fluxes at sea. *Bound.-Layer Meteor.,* **95,** 271–302.

Pedreros, R., G. Dardier, H. Dupuis, H. C. Graber, W. M. Drennan, A. Weill, C. Guérin, and P. Nacass, 2003: Momentum and heat fluxes via the eddy correlation method on the R/V *L'Atalante* and an ASIS buoy. *J. Geophys. Res.,* **108,** 3339, doi:10.1029/2002JC001449.

Phelps, G. T., and S. Pond, 1971: Spectra of the temperature and humidity fluctuations and of the fluxes of moisture and sensible heat in the marine boundary layer. *J. Atmos. Sci.,* **28,** 918–928.

Raupach, M. R., 1981: Conditional statistics of Reynolds stress in rough-wall and smooth-wall turbulent boundary layers. *J. Fluid Mech.,* **108,** 363–382.

Rutgersson, A., A. Smedman, and U. Högström, 2001a: Use of conventional stability parameters during swell. *J. Geophys. Res.,* **106,** 27 177–27 134.

——, ——, and A. Omstedt, 2001b: Measured and simulated latent and sensible heat fluxes at two marine sites in the Baltic Sea. *Bound.-Layer Meteor.,* **99,** 53–84.

Saïd, F., and A. Druilhet, 1991: Experimental study of the atmospheric marine boundary layer from in-situ aircraft measurements (TOSCANE-T Campaign): Variability of boundary conditions and eddy flux parameterization. *Bound.-Layer Meteor.,* **57,** 219–249.

Schmitt, K. F., C. A. Frihe, and C. H. Gibson, 1979: Structure of marine surface layer turbulence. *J. Atmos. Sci.,* **36,** 602–618.

Schotanus, P., F. T. M. Nieuwstadt, and H. A. R. De Bruin, 1983:

Temperature measurement with a sonic anemometer and its application to heat and moisture fluxes. *Bound.-Layer Meteor.,* **26,** 81–93.

Sempreviva, A. M., and S.-E. Gryning, 1996: Humidity fluctuations in the marine boundary layer measured at a coastal site with an infrared humidity sensor. *Bound.-Layer Meteor.,* **77,** 331–352.

Smedman, A., U. Högström, H. Bergström, A. Rutgersson, K. Kahma, and H. Pettersson, 1999: A case study of air–sea interaction during swell conditions. *J. Geophys. Res.,* **104,** 25 833–25 851.

——, X. Guo-Larsén, U. Högström, K. K. Kahma, and H. Pettersson, 2003: Effects of sea state on the momentum exchange over the sea during neutral conditions. *J. Geophys. Res.,* **108,** 3367, doi:10.1029/2002JC001526.

——, U. Högström, J. C. R. Hunt, and E. Sahlée, 2007a: Heat/mass transfer in the slightly unstable atmospheric surface layer. *Quart. J. Roy. Meteor. Soc.,* **133,** 37–51.

——, ——, E. Sahlée, and C. Johansson, 2007b: Critical reevaluation of the bulk transfer coefficient for sensible heat over the ocean during unstable and neutral conditions. *Quart. J. Roy. Meteor. Soc.,* **133,** 227–250.

Smith, S. D., and R. J. Anderson, 1984: Spectra of humidity, temperature, and wind over the sea at Sable Island, Nova Scotia. *J. Geophys. Res.,* **89,** 2029–2040.

Sullivan, P. P., J. B. Edson, J. C. McWilliams, and C.-H. Moeng, 2004: Large-eddy simulations and observations of wave-driven boundary layers. Preprints, *16th Symp. on Boundary Layers and Turbulence,* Portland, ME, Amer. Meteor. Soc., 8.12.

Webb, E. K., G. I. Pearman, and R. Leuning, 1980: Correction of flux measurements for density effects due to heat and water vapour transfer. *Quart. J. Roy. Meteor. Soc.,* **106,** 85–100.

Willmarth, W. W., and S. S. Lu, 1974: Structure of the Reynolds stress and the occurrence of bursts in the turbulent boundary layer. *Advances in Geophysics,* Vol. 18A, Academic Press, 287–314.

Zhang, W., W. Perrie, and W. Li, 2006: Impact of waves and sea spray on midlatitude storm structure and intensity. *Mon. Wea. Rev.,* **134,** 2418–2442.